Fundamental Methods to Measure the Orbital Angular Momentum of Light

Berkhout, G.C.G.

CHAPTER 8

Towards applications based on measuring the orbital angular momentum of light

Efficient measurement of the orbital angular momentum (OAM) of light has been a long-standing problem in both classical and quantum optics. In this thesis, we have presented two ways to solve this problem, thus opening the way for applications based on the OAM of light. In previous chapters, we have identified large bandwidth optical communication and the detection of OAM in astrophysics as potential applications. The application of OAM generation and detection will, in general, involve more complex types of light than the monochromatic, coherent laser light that we used to test our detection methods. In this final chapter, we take the first steps towards the development of such applications by addressing two important aspects of detecting OAM in real applications. First we study the response of both detection systems to polychromatic and (partially) incoherent light. Secondly, we study the orthogonality of the output states in one of our detection systems, the mode sorter, and its response to single photons, which are both relevant for applications in large bandwidth optical communication. These first assessments reveal important properties of the OAM detection systems, that, amongst many other aspects, have to be studied in more detail in the development of applications.

8.1 Introduction

Ever since it was found in 1992 that light can carry orbital angular momentum [1], many efforts have been made to measure this quantity, both for beams of light as well as for single photons. A number of different measurement schemes has been described in the literature. It was, for instance, already known before 1992, that one can find wave front dislocations, or optical vortices, in a speckle pattern by interfering the pattern with a flat wave front, such that the optical vortices show up as a characteristic fork-like interference pattern [8]. The OAM of a Laguerre-Gaussian beam is directly linked to the topological charge of the optical vortex at its centre and the interference method can therefore be used to measure this OAM [53]. It does, however, require many photons to be in the same OAM state to build up the interference pattern. Another way to measure the OAM of a light beam is to use special apertures like the multi-pinhole interferometer (MPI) [27] or a triangular aperture [55], that create qualitatively different diffraction patterns for light in different OAM states. Again this requires many photons to be in the same state. One can also use specific holograms to sort orbital angular momentum states spatially [33, 54], but only with an efficiency that is approximately equal to $1/N$, where N is the number of detected states and one again needs many photons to be in the same state.

There are also methods to measure the OAM of a single photon. One of these methods is to test if a single photon is in a specific state or not, by means of a hologram and a single mode fibre [29]. By repeating this test with a series of different holograms, one can build up a statistical average of the OAM states of the input photons. For a single photon, this measurement discriminates between two states and does not benefit from the infinite nature of the OAM state space. The first measurement to discriminate between more than two OAM states for a single photon was described by Leach et al. [13], who used a Mach-Zehnder interferometer combined with a Dove prism to spatially sort photons based on their OAM. The experiment showed the sorting of four OAM states. In order to sort more states, interferometers have to be added to the setup. To sort N different states, one needs $N-1$ Mach-Zehnder interferometers, which is experimentally very challenging. In chapters 6 and 7 of this thesis, we have presented a different scheme to sort OAM states, that is much easier to set up since it consists of only two custom optical elements and two lenses. This mode sorter converts N different input OAM states into N spatially separated output spots, where N is limited only by the accuracy of the optics. The only disadvantage of this system is that the output spots slightly overlap, which limits the accuracy by which one can determine the OAM of a single photon. This can, however, be overcome by modifying the design of the two custom optical elements, an example of which has been given in chapter 6.

The MPI and the mode sorter presented in this thesis have made measuring the OAM of a light beam experimentally much more feasible; in the case of the mode sorter it even works for single photons. This opens the way towards applications of the OAM of light. So far, we have only treated the case of coherent, monochromatic light. Several times

however, we have hinted at the possiblity of detecting OAM in light from astrophysical sources and the possibility of astrophysical sources generating light with orbital angular momentum has been treated elsewhere [11, 26, 71]. Light from astrophysical sources will, in general, not be monochromatic and coherent. It is therefore crucial to study the response of both the MPI and the mode sorter to polychromatic and (partially) incoherent light. The idea that partially coherent light can carry OAM has been described extensively in literature [72–76]. It has also been shown that a special class of partially incoherent light beams can, perhaps surprisingly, still produce diffraction patterns with true intensity zeros behind a MPI [18, 42].

A second application of the OAM of light mentioned in this thesis, is its use for high dimensional communication schemes, which has been discussed in the literature [30, 33]. Our mode sorter can form a key part of this application, provided the different OAM states can be separated sufficiently well. In this chapter, we study the channel separation and the response of the mode sorter for single photons.

This chapter provides calculations for relatively simple examples of polychromatic and (partially) incoherent light and is organised as follows. We treat the MPI and the mode sorter in section 8.2 and section 8.3, respectively. In the latter section, we also study the channel separation of the mode sorter and its response in the quantum regime, with concluding remarks in section 8.4.

8.2 Multi-pinhole interferometer

8.2.1 Response to polychromatic light

All results presented in previous chapters were obtained with a helium-neon laser, that has a wavelength $\lambda = 632.816\,\text{nm}$. Due to thermal expansion of the laser cavity this frequency can vary by only $\Delta\lambda = \pm 0.001\,\text{nm}$, being limited by the small spectral width of the optical gain. This has a very minute effect on the diffraction pattern behind a multi-point interferometer (MPI), as can be easily seen by considering an $N = 2$ MPI, which is Young's double slit experiment with the slits replaced by pinholes. The far-field diffraction pattern behind the $N = 2$ MPI is given by bright bands on a dark background separated by a distance Δx, which is given by

$$\Delta x = \frac{\lambda z}{2a}, \tag{8.1}$$

where z is the distance from the MPI to the detector and a is the distance from the pinholes to the centre of the MPI. It should be noted that the diffraction pattern scales with λz.

The diffraction patterns behind a general MPI have been extensively discussed in chapter 2 and 3. For $N \geq 4$, they contain information on the topological charge of an impinging optical vortex. These diffraction patterns can be analysed qualitatively by looking at their numerical Fourier transform [41]. This Fourier transformed image shows $2N$

copies of the MPI, that are scaled with respect to the original. For odd N, one can directly determine the relative phase of the incident optical field at each pinhole by determining the phase of the Fourier transformed image at the vertices of one of these copies of the MPI. In addition we can also derive the relative amplitudes of the fields at the individual pinholes, as shown in chapter 5. The radius of the MPI in the Fourier transform, r, and the size of the pinholes, s, are given by

$$r = \frac{n_{\sim} da}{\lambda z_{\sim}}, \tag{8.2}$$

$$s = \frac{n_{\sim} db}{\lambda z_{\sim}}, \tag{8.3}$$

where $n_{\sim}$ is the number of pixels in the original image, d the pixel size, a and b the separation and the diameter of the pinholes in the MPI respectively, λ the wavelength and $z_{\sim}$ the propagation distance. In [41], Guo *et al.* state that the phase of the field can be unambiguously determined if the separation between the pinholes is at least two times their diameter. This can be easily understood from the above equation, since for smaller separations the pinholes will overlap in the Fourier transformed image and the phase cannot be unambiguously determined.

As can be seen from equation 8.2, the positions and sizes of the pinholes in the Fourier transformed image not only depend on the separation and diameter of the pinholes in the MPI, but also on the wavelength. If the field impinging on the MPI contains light of multiple wavelengths, the Fourier transformed image will be the addition of images of the pinholes for different wavelengths.

In order to demonstrate this point, we simulated the diffraction pattern behind an MPI for several different input fields. The patterns are shown in figure 8.1 and were recorded behind the same $N = 5$ MPI with $a = 200\,\mu m$, $b = 50\,\mu m$, recorded at $z_{\sim} = 0.1$ m. We have simulated the diffraction pattern for three different wavelengths, $\lambda = 633$ nm, $\lambda = 700$ nm and $\lambda = 780$ nm, and superpositions thereof. To be able to more clearly distinguish the individual modes in the superpositions, we gave the modes a different topological charge. Although this is somewhat artificial, it simulates a superposition of wavelengths and modes and therefore helps to illustrate our point more clearly.

As in previous chapters, we analyse the diffraction patterns by calculating the numerical Fourier transform of the diffraction patterns. Figure 8.2 shows the absolute value of this Fourier transform for the diffraction patterns shown in figure 8.1. As explained before, one can see 10 pentagons in the Fourier transform, where some of the points are shared between two pentagons. The size of these pentagons decreases when the wavelength increases (compare figure 8.2 (a) and (b)). As expected, a superpositions of the patterns for two wavelengths results in the superposition of the two Fourier transformed images. In figure 8.2 (c) these two patterns can still be distinguished, but in figure 8.2 (d), where the wavelengths are closer together, the points start overlapping.

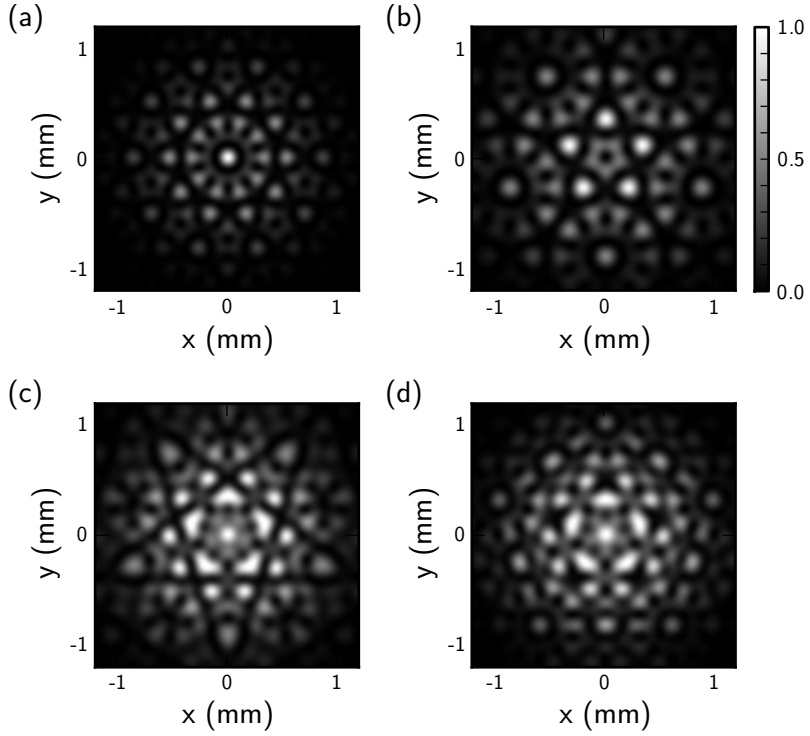

Figure 8.1: Diffraction patterns behind an $N = 5$ MPI. The parameters for the MPI are the same for all four images, but the wavelength of the light is varied. (a) $\lambda = 633$ nm with $\ell = 0$, (b) $\lambda = 780$ nm with $\ell = -1$, (c) a superposition of (a) and (b), and (d) a superposition of (a) and $\lambda = 700$ nm with $\ell = -1$.

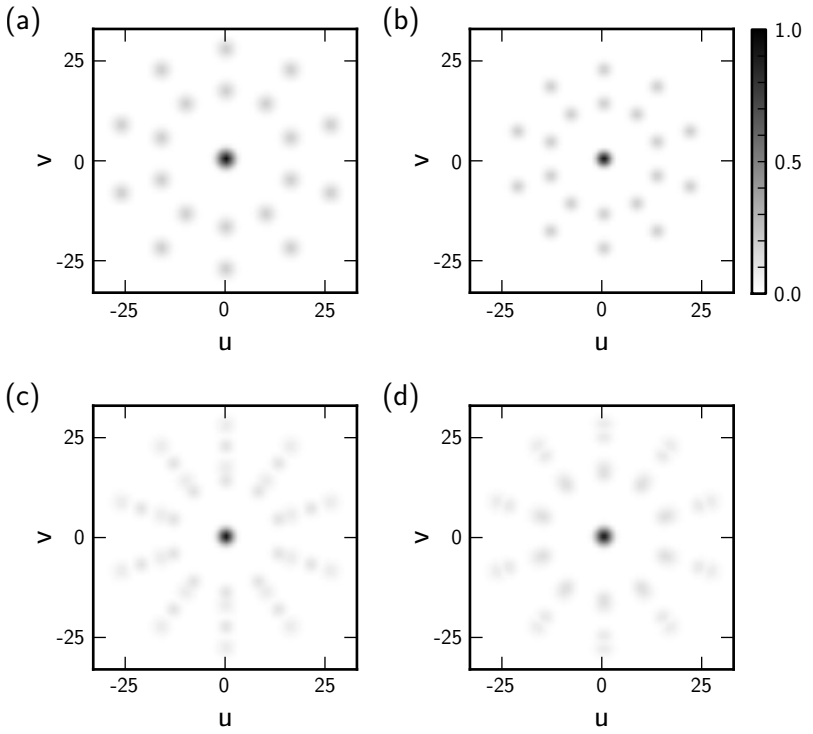

Figure 8.2: Absolute value of the numerical Fourier transform of the diffraction patterns shown in figure 8.1.

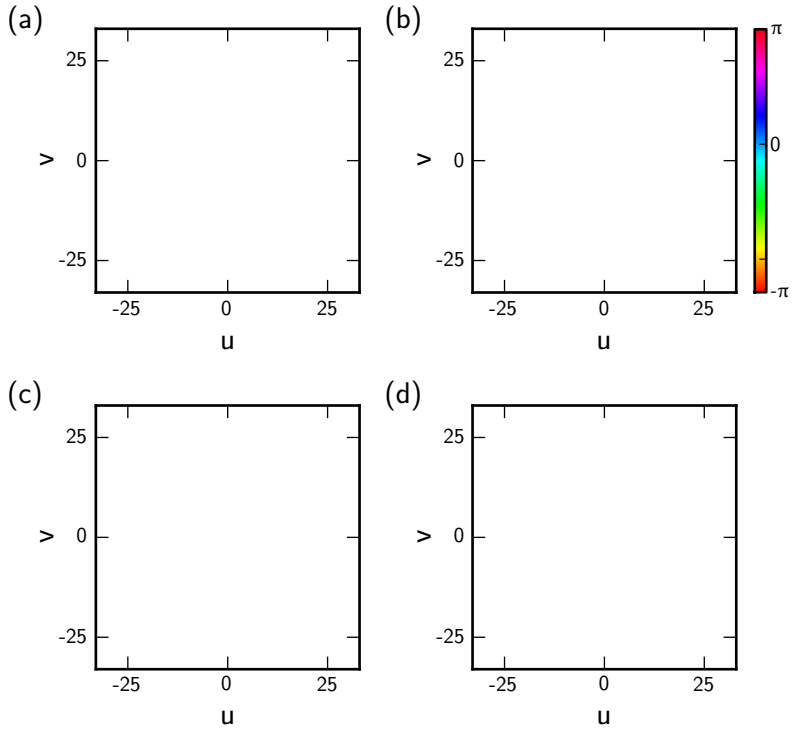

Figure 8.3: Phase of the numerical Fourier transform of the diffraction patterns shown in figure 8.1.

Figure 8.3 shows the phase of the Fourier transform and illustrates the overlap even better. One can clearly see that the phase is equal at all the pinholes for figure 8.3 (a) and increases from 0 to 2π in figure 8.3 (b). In figure 8.3 (c), one can still distinguish the two different wavelengths, but this is impossible in figure 8.3 (d), where the different pinholes overlap and the phase is blurred.

It depends on the exact source that is studied, how stringent the requirement on the wavelength is. If the source emits a spectrum that consists of several frequency lines that are not related, the vorticity can only be determined if the resulting peaks in the Fourier transform do not overlap. The required wavelength separation is then given by

$$\frac{\Delta\lambda}{\lambda} = \frac{2b}{4a\sin(\pi/N) - b}. \tag{8.4}$$

The size of the pinholes should be kept as small as possible to allow for a large wavelength range to be detectable. If the MPI is illuminated by a spectrum of different wavelengths, the analysis will return a blurred Fourier transformed image. If all different wavelengths contain a vortex, or in other words, if the input field is a white light vortex [77], the

analysis will still return this vorticity and the method is adequate. In other cases, one has to be careful in interpreting the image.

8.2.2 Partial coherence

As mentioned before, it has been show that partially coherent light can still contain optical vortices and possess orbital angular momentum [72–76]. The aim of this section is to find out if an MPI is able to detect the vorticity in such a field. Intuitively, one would think that this is not the case, since the interference patterns is washed out by the (partial) incoherent character of the beam. However, Gbur *et al.* show that special types of partially coherent beams can generate diffraction patterns with true intensity zeroes [18]. Below we give an analysis that is based on the one presented by Gbur, but for a single wavelength. The interference pattern behind N pinholes is given by

$$I(x,y) \propto \mathbf{r}^{(N)\dagger}\mathbf{M}^{(N)}\mathbf{r}^{(N)}, \tag{8.5}$$

where

$$\mathbf{r}^{(N)} = \begin{pmatrix} A_1 e^{i\phi_1} \\ A_2 e^{i\phi_2} \\ \dots \\ A_N e^{i\phi_N} \end{pmatrix}, \tag{8.6}$$

with A_j the amplitude of the optical field at the j-th pinhole and $\phi_j \equiv kR_j$ is the phase introduced by the distance R_j between the pinhole and the observation point (x,y). The matrix $\mathbf{M}^{(N)}$ is given by

$$\mathbf{M}^{(N)} = \begin{pmatrix} 1 & \mu_{12} & \dots & \mu_{1N} \\ \mu_{12}^* & 1 & \dots & \mu_{2N} \\ \vdots & \vdots & \ddots & \vdots \\ \mu_{1N}^* & \mu_{2N}^* & \dots & 1 \end{pmatrix}, \tag{8.7}$$

where

$$\mu_{jk} = \frac{\langle A_j^* A_k \rangle}{\sqrt{I_j I_k}} \tag{8.8}$$

is the spectral degree of coherence and I_j would be the intensity observed if only the j-th pinhole would be open and the average is taken over an ensemble of space–frequency realizations of the field. The important parameter is the matrix $\mathbf{M}^{(N)}$, which describes the degree of coherence between each of the pinholes. The case of fully coherent beams, i.e. $\mu_{jk} = 1$ for all j,k has been described extensively in previous chapters. If not all μ_{jk} are equal to 1, the diffraction pattern will be partly washed out. In the case $N = 2$, this results in a pattern that does not contain any intensity zeroes. Gbur shows that for $N > 2$ and special classes of partially coherent beams, the intensity patterns will still contain

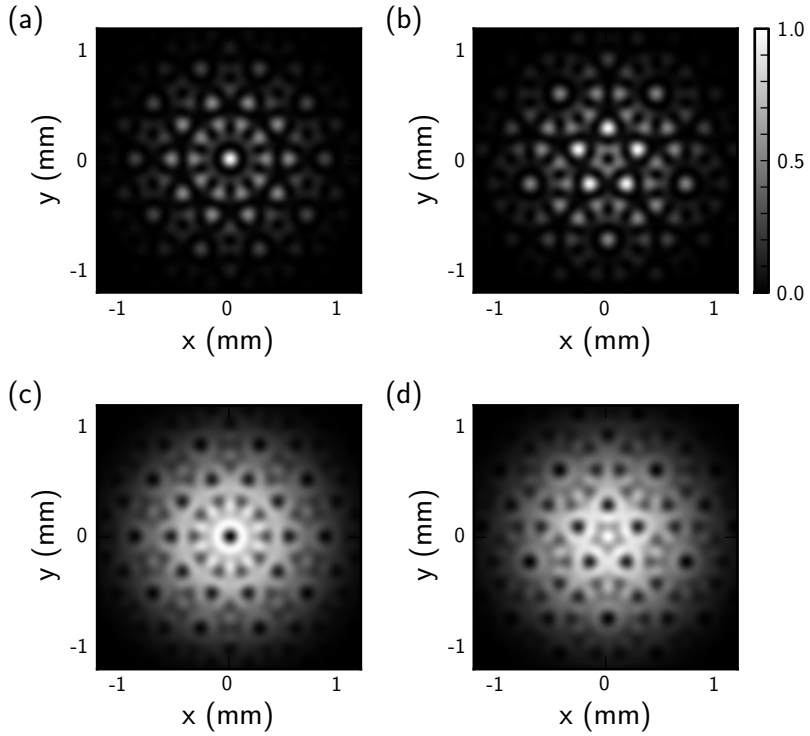

Figure 8.4: Diffraction patterns behind an $N = 5$ MPI for different types of input beams. (a) Coherent beam $l = 0$, (b) coherent beam $\ell = -1$, partially incoherent beam $\ell = 0$ satisfying equation 8.9 and (d) partially incoherent beam $\ell = -1$ satisfying equation 8.9. All other parameters are equal for all images.

intensity zeroes. One of these special cases is the case where all μ_{jk} are real and equal for $j \neq k$ and $\mu_{jj} = 1$ and

$$\mu = -\frac{1}{N-1}. \tag{8.9}$$

By comparing the diffraction patterns with the diffraction patterns obtained in previous chapters, one can see that these patterns are in fact equal, but with the colours inverted (see figure 8.4).

We also study intermediate cases by varying μ between 1 and $-\frac{1}{N-1}$. Figure 8.5 shows diffraction patterns for several values of μ. We believe that it is justified to conclude that, except for the fully incoherent case, all patterns contain a remainder of the pattern for the fully coherent case. This can be understood by the idea that a partially coherent beam can be considered as having a fully coherent part and a fully incoherent part. The fully coherent part will result in a diffraction pattern as studied in chapter 2 and the incoherent part will result in a uniform background. Applying the Fourier analysis, as described before, shows that this idea is justified. The Fourier transformed images are

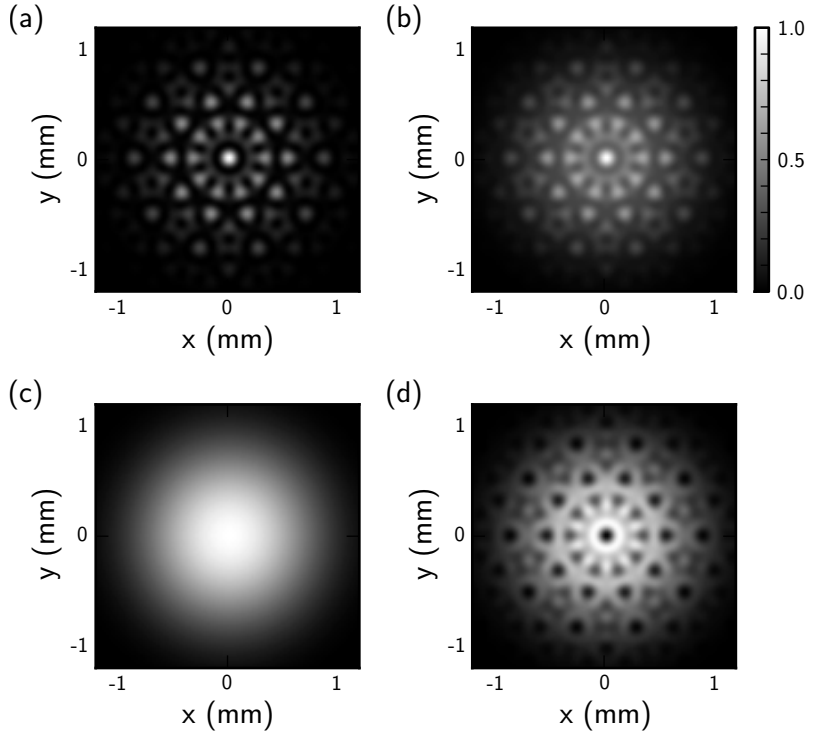

Figure 8.5: Diffraction patterns behind an $N = 5$ MPI for beams with different coherence. (a) Fully coherent beam $\mu = 1$, (b) $\mu = \frac{1}{N-1}$, (c) incoherent beam $\mu = 0$ and (d) $\mu = -\frac{1}{N-1}$. All other parameters are equal for all images.

comparable to the ones presented, for instance, in figure 8.2 and 8.3 (a) and (b), the only noticeable difference being that the central pixel has a larger amplitude due to the fact that all incoherent contributions end up in this pixel. The only exception is the case that $\mu_{jk} = 0$, or, in other words, the case of fully incoherent light, where the diffraction pattern is completely washed out.

8.3 Mode sorter

8.3.1 Monochromaticity

The OAM mode sorter that is extensively described in chapters 6 and 7 separates optical vortex states by transforming them to inclined plane waves, which are in turn focussed to different positions on a detector by a standard lens. The two custom optical elements that are needed to perform the transformation are created using two spatial light modulators (SLMs). The main advantage of SLMs is their flexibility to add any desired phase profile to an incoming beam. The phase profiles of the aforementioned custom optical

components are described by (see chapter 6)

$$\phi_1(x,y) = \frac{2\pi a}{\lambda f}\left[y\arctan\left(\frac{y}{x}\right) - x\ln\left(\frac{\sqrt{x^2+y^2}}{b}\right) + x\right], \tag{8.10}$$

$$\phi_2(u,v) = -\frac{2\pi ab}{\lambda f}\exp\left(-\frac{u}{a}\right)\cos\left(\frac{v}{a}\right). \tag{8.11}$$

In addition, the SLMs can be used to compensate for any aberrations or misalignment in the optical setup. The SLMs used in chapter 6 and 7 are reflective devices and their main disadvantage is their low reflectivity. Especially when combined with the beam splitters, that are used to ensure perpendicular incidence on the SLMs, the overall throughput of the mode sorter is low, typically about 1%. An alternative is to make the two custom components out of a transparent material like glass or plastic. The thickness profiles of the optical components then needs to be of the following form

$$t_1(x,y) = \frac{\lambda\phi_1(x,y)}{2\pi(n-1)}, \tag{8.12}$$

$$t_2(u,v) = \frac{\lambda\phi_2(u,v)}{2\pi(n-1)}, \tag{8.13}$$

where n is the refractive index of the material. In other words

$$t_1(x,y) = \frac{a}{f(n-1)}\left[y\arctan\left(\frac{y}{x}\right) - x\ln\left(\frac{\sqrt{x^2+y^2}}{b}\right) + x\right], \tag{8.14}$$

$$t_2(u,v) = -\frac{ab}{f(n-1)}\exp\left(-\frac{u}{a}\right)\cos\left(\frac{v}{a}\right). \tag{8.15}$$

Conveniently, these thickness profiles are independent of the wavelength of the input light, provided that the dispersion of the glass is negligible, which can be achieved with special types of glass over a fairly large range of wavelengths. The fact that the optics can operate at different wavelengths makes them extremely suitable for applications in high-dimensional optical communication.

8.3.2 Partial coherence

The orbital angular momentum of partially coherent light is still well defined and each photon has a well defined orbital angular momentum when measured. Since the mode sorter focusses individual photons to a position on the detector depending on the orbital angular momentum of the photon, the mode sorter still works for partially coherent light. The mode sorter can therefore be used to measure OAM spectrum of a partially coherent light beam.

8.3.3 Orthogonality

One disadvantage of the OAM mode sorter is the fact that the spatially separated output spots slightly overlap for different OAM states. In this section we further study this lack of orthogonality or separability, which introduces cross-talk between the states.

In the mode sorter based on spatial light modulators that is described in chapter 6 and 7, the output aperture of the mode sorter is square and completely filled by the transformed beam. As explained in chapter 7, there is no information about the OAM state in the one of the two transformed axes, so we will treat this problem as being one-dimensional. If we assume that the lens that focusses the transformed OAM states is much larger than the output aperture of the mode sorter, the focussed spots will have a intensity profile, $I(\alpha)$, determined by this square aperture

$$I(\alpha) \propto \left(\frac{\sin(\alpha)}{\alpha} \right)^2, \tag{8.16}$$

where $\alpha = \frac{kd}{2f}(x - x_\ell), k = \frac{2\pi}{\lambda}$ is the wavenumber, λ the wavelength, d the aperture size, f the focal length and $x_\ell = \frac{\lambda f}{d}$ is the central position of the ℓ-th peak. The focussed peaks will slightly overlap, which is inherent to the optical design. One could argue that increasing the size of the aperture d would decreases the width of the spots. This does however also decreases the separation between the spots and the overlap will remain the same. The same reasoning holds for changing the focal length of the final lens. To further support this argument we present a numerical study of this system.

The most convenient way to use a mode sorter in a communication scheme would be to define regions of interest in its focal plane. If a photon hits the detector in a specific region, we can link this position to an orbital angular momentum. We define the ℓ-th region such that its centre coincides with the peak position for the ℓ-th mode. The width of one region is given by the separation of the two peaks and so

$$x_\ell - \frac{\lambda f}{2d} < x \leq x_\ell + \frac{\lambda f}{2d}. \tag{8.17}$$

Since $\sin(\alpha)/\alpha$ cannot be integrated analytically, we numerically evaluate the problem. First of all, we calculate the intensity in each of the defined regions for an input beam with $\ell = 0$. About 80% of the intensity ends up in the correct beam while the other 20% is spread out over the other bins, mostly the neighbouring ones.

To determine whether the overlap indeed does not depend on f or on d, we have calculated the intensity in all regions for several values of these parameters. As expected there is indeed no dependence.

As shown in the previous chapter, the mode sorter is sensitive to superpositions of modes. In addition the relative phase between modes is preserved. This relative phase does, however, alter the exact intensity distribution and therefore the intensity recorded

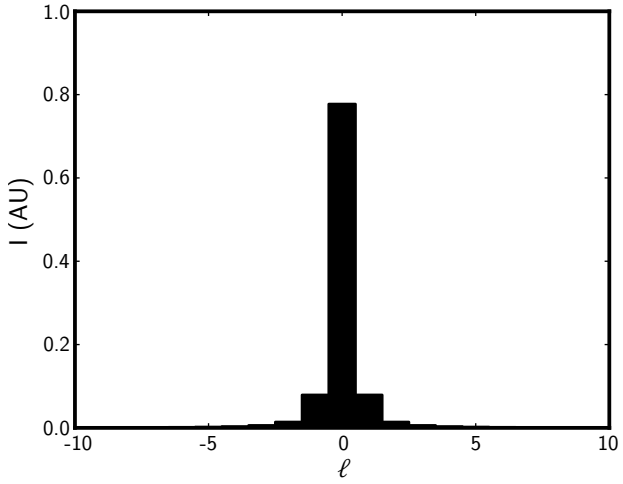

Figure 8.6: Intensity in each of the regions when illuminated with a pure $\ell = 0$ optical vortex.

in the defined bins. To study the effect of this relative phase, we have numerically studied an equal superposition of two modes, $\ell = -1$ and $\ell = 0$, where we vary the relative phase. Figure 8.7 shows the intensity in one of the regions, the one corresponding to either $\ell = -1$ or $\ell = 0$, which are equal since the problem is symmetric. As expected the intensity in the regions depends on the relative phase between the modes.

The variation is significant, about 20% of the peak value and this is something that needs to be taken into account, since it can affect the outcome of the measurements. The relative phase is also affected by the exact angular orientation of the mode sorter. A possible solution to this dependence on the relative phase is to use only pure modes and keep their relative phase fixed.

8.3.4 Quantum optics

Decreasing the intensity of the input beam does not change the working principle of the mode sorter and thus it should able to sort individual photons. The restriction that the spatially separated output spots slightly overlap leaves some inaccuracy in the determination of the OAM value of the photon. This can be resolved by modifying the optical design by adding a binary grating to the first optical element of the mode sorter and changing the second custom element accordingly. This will create a number of diffraction orders, all containing the same phase ramp. By changing the periodicity of the grating, these phase ramps can be connected to form a higher phase ramp, thereby increasing the separation between the final spots. Implementing this, does increase the overall optical complexity of the system.

In an optical communication scheme, one could also use only every second, third or even fourth mode. The latter option reduces the overlap between different output states

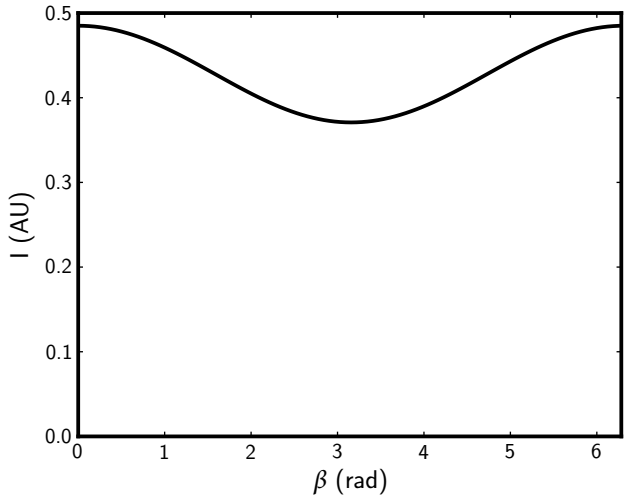

Figure 8.7: Intensity in the $\ell = 0$ region for an equal superposition of $\ell = -1$ and $\ell = 0$, $A \propto e^{-i\phi} + e^{i\beta}$ as a function of relative phase between the modes, β.

to below the 1% level.

As the orbital angular momentum states are spatially separated in the focus of the mode sorter, this allows us to perform operations on the individual modes in a spectrum, like changing the relative phase and amplitudes. This can also have applications in more fundamental studies of OAM.

One could use the same mode sorter, but inverted, to generate OAM states and superpositions thereof.

8.4 Conclusion

For almost twenty years, efficient measurement of the orbital angular momentum of light has been experimentally challenging. In this thesis we have presented two novel methods to solve this measurement problem, which open the way for use of the OAM of light in applications. These applications will bring new challenges like measuring the OAM of polychromatic and (partially) incoherent light. In this final chapter we have shown with some initial calculations that the multi-pinhole interferometer is able to detect the OAM of an incoming light beam with a limited wavelength range and that it still works for partially incoherent light. In addition, we have shown that the mode sorter works for both polychromatic and partially coherent light. Finally, we have shown that the inherent cross-talk in the mode sorter can be reduced by changing the optical design. All these aspects of the applications of orbital angular momentum detection are very interesting and the initial calculations presented here can serve as a starting point for more detailed study.